THE ASTROPHYSICAL JOURNAL, 528:436–444, 2000 January 1
© 2000. The American Astronomical Society. All rights reserved. Printed in U.S.A.

ASCA OBSERVATIONS OF THE YOUNG ROTATION-POWERED PULSARS PSR B1046−58 AND PSR B1610−50

M. J. PIVOVAROFF AND V. M. KASPI
Department of Physics and Center for Space Research, Massachusetts Institute of Technology, Cambridge, MA 02139; mjp@space.mit.edu, vicky@space.mit.edu

AND

E. V. GOTTHELF
Columbia Astrophysics Laboratory, Columbia University, 550 West 120th Street, New York, NY 10027; evg@astro.columbia.edu
Received 1998 November 23; accepted 1999 August 16

ABSTRACT

We present X-ray observations of two young energetic radio pulsars, PSRs B1046−58 and B1610−50, and their surroundings, using archival data from the *Advanced Satellite for Cosmology and Astrophysics* (*ASCA*). The energetic pulsar PSR B1610−50 is detected in X-rays with a significance of 4.5 σ. The unabsorbed flux, estimated assuming a power-law spectrum and a neutral hydrogen column density $N_{\rm H}$ of 5×10^{21} cm^{-2}, is $(2.5 \pm 0.3) \times 10^{-13}$ ergs cm^{-2} s^{-1} in the 2–10 keV band. Pulsed emission is not detected; the pulsed fraction is less than 31% at the 90% confidence level for a 50% duty cycle. We argue that the emission is best explained as originating from a pulsar-powered synchrotron nebula. The X-ray counterpart of the pulsar is the only hard source within the 95% error region of the previously unidentified γ-ray source 3EG J1048−5840. This evidence supports the results of Kaspi et al., who suggest, in a companion paper, that PSR B1046−58 is the counterpart to 3EG J1048−5840. X-ray emission from PSR B1610−50 is not detected. Using assumptions similar to those above, the derived 3 σ upper limit for the unabsorbed 2–10 keV X-ray flux is 1.5×10^{-13} ergs cm^{-2} s^{-1}. We use the flux limit to estimate the pulsar's velocity to be less than $\sim$170 km s^{-1}, casting doubt on a previously reported association between PSR B1610−50 and supernova remnant Kes 32. Kes 32 is detected, as is evident from the correlation between X-ray and radio emission. The *ASCA* images of PSR B1610−50 are dominated by mirror-scattered emission from the X-ray–bright supernova remnant RCW 103, located 33′ away. We find no evidence for extended emission around either pulsar, in contrast to previous reports of large nebulae surrounding both pulsars.

Subject headings: gamma rays: observations — pulsars: individual (PSR B1046−58, PSR B1610−50) — stars: neutron — supernova remnants — X-rays: stars

1. INTRODUCTION

X-ray observations of radio pulsars provide a powerful diagnostic of the energetics and emission mechanisms of rotation-powered neutron stars. As magnetic dipole braking slows the pulsar, it loses rotational kinetic energy at a rate $\dot{E} = 4\pi^2 I \dot{P} P^{-3}$, where I is the moment of inertia of the neutron star, assumed to be 10^{45} g cm^2, and P is the rotation period. Though pulsars have traditionally been most easily studied at radio wavelengths, only a small fraction (10^{-7} to 10^{-5}) of the "spin-down luminosity" $\dot{E}$ manifests itself as radio pulsations. Instead, it is believed that a significant fraction of the luminosity emerges as a relativistic wind of positrons and electrons.

When this wind is confined by the surrounding medium, an observable synchrotron nebula results. Measurements of the morphology and spectrum are essential for determining the content and energy spectrum of the wind, probing the ambient density, and understanding the shock acceleration mechanism. The growing list of observable X-ray–emitting rotation-powered pulsars allows the study of the properties of the population as a whole. Young pulsars constitute a particularly interesting subset to investigate owing to their large spin-down luminosities ($\gtrsim 10^{36}$ ergs s^{-1}).

PSR B1046−58 was discovered by Johnston et al. (1992) during a 1400 MHz survey of the Galactic plane for radio pulsars. PSR B1046−58 has $\dot{E} = 2.0 \times 10^{36}$ ergs s^{-1}, characteristic age $\tau_C \equiv P/2\dot{P} = 20$ kyr, and properties reminiscent of the Vela pulsar. The dispersion measure (DM) toward the pulsar is 129 pc cm^{-3}. Using the Taylor & Cordes (1993) DM-distance relationship, the distance to PSR B1046−58 is estimated to be $d \approx 3.0$ kpc. The large $\dot{E}/4\pi d^2$ value (a useful indicator of the detectability of its putative pulsar wind nebula) make it a strong candidate for X-ray emission. Kaspi et al. (2000) have found evidence for γ-ray pulsations from an EGRET point source spatially coincident with PSR B1046−58.

PSR B1610−50 was also discovered in the Johnston et al. survey. PSR B1610−50 is the fourth youngest Galactic pulsar ($\tau_c = 7.4$ kyr) and has $\dot{E} = 1.6 \times 10^{36}$ ergs s^{-1} and DM = 586 pc cm^{-3}. PSR B1610−50 occupies an interesting position in the age phase-space of known pulsars: its age is between those of the youngest pulsars ($\tau_c \lesssim 2$ kyr), like the Crab and PSR B0540−69, and those in their "adolescence" ($\tau_c \sim$ 10–20 kyr), like Vela and PSR B1046−58. Caraveo (1993) proposed that PSR B1610−50 is associated with the nearby supernova remnant Kes 32. However, using the DM-derived distance of 7.3 kpc and assuming the system's age is τ_c, the pulsar's implied transverse velocity is $v_t > 2300(d/7.3)$ km s^{-1}, significantly higher than the mean pulsar velocity (e.g., Lyne & Lorimer 1994). If it is traveling at so high a speed, one might expect strong ram-pressure confinement of its wind and a correspondingly high X-ray luminosity from the resultant synchrotron emission (see, e.g., Cheng 1983; Wang, Li, & Begelman

1993; Finley, Srinivasan, & Park 1996; Romani, Cordes, & Yadigaroglu 1997; Wang & Gotthelf 1998).

Table 1 presents information for PSR B1046−58 and PSR B1610−50 including position, spin parameters, and derived quantities (i.e., spin-down luminosity and characteristic age).

Previous X-ray work on PSRs B1046−58 and B1610−50 has been limited in scope. Becker & Trümper (1997) published a *ROSAT*-band (0.1–2.4 keV) luminosity for PSR B1046−58 of 4×10^{32} ergs s^{-1} but gave no further analysis. Kawai, Tamura, & Saito (1998) presented *ASCA* data on both pulsars but restrict their attention to a single Gas Imaging Spectrometer (GIS) image of each pulsar. For both PSRs B1046−58 and B1610−50, they reported the detection of a large nebula (tens of arcminutes) associated with each pulsar. This paper undertakes a detailed analysis of the archival *ASCA* data, with an emphasis on image analysis.

2. OBSERVATIONS

ASCA (Tanaka, Inoue, & Holt 1994) observed PSR B1046−58 on 1994 January 27 and PSR B1610−50 on 1994 March 25. We present an analysis of the data obtained from the public archive. For both observations, data were taken with all four imaging spectrometers, each in the focal plane of its own foil mirror: two Solid State Imaging Spectrometers (SIS-0, SIS-1) employing charge-coupled devices (CCDs), and two Gas Imaging Spectrometers (GIS-2, GIS-3) employing gas scintillation proportional counters. These spectrometers offer moderate energy ($\sim$5%) and imaging ($\sim 2'$) resolution in their $\sim$1–10 keV energy bandpass. The SIS has superior imaging and spectral capabilities, while the GIS has a higher effective area above $\sim$2 keV and a greater net observation time than the SIS. To facilitate pulsation searches, GIS data were collected in the highest time resolution configuration (0.488 or 3.906 ms depending on data acquisition rate). SIS data were acquired in 4 CCD mode with 16 s integrations (PSR B1046−58) and 2 CCD mode with 8 s integrations (PSR B1610−50) using a combination of FAINT and BRIGHT modes (see the *ASCA* Data Analysis Guide for details). The data were filtered to exclude times of high background contamination using the standard "REV2" screening criteria. This rejects time intervals of South Atlantic Anomaly passages, Earth block, bright Earth limb in the field of view, and periods of high particle activity. The resulting effective observation times per single detector are 18 ks (GIS) and 15 ks (SIS) for PSR B1046−58 and 11 ks (GIS) and 8.4 ks (SIS) for PSR B1610−50.

3. PSR B1046−58

3.1. *Image Analysis*

3.1.1. *ASCA Data*

Flat-fielded images were generated by aligning and coadding exposure-corrected images from the pairs of instruments. Exposure maps were generated with ASCAEXPO, *ASCA* software that uses the satellite aspect solution, instrument map (GIS), chip alignment, and hot pixel map (SIS) to determine the exposure time for each sky image pixel. The exposure correction was highly effective in removing the GIS instrumental structure due to the window support grid. Figure 1 (*top left*) displays the resultant smoothed broadband (0.8–10 keV) image for the GIS. The image reveals emission confined to a slightly oval $\sim 4' \times 7'$ region, elongated along the direction parallel to declination. Though the statistics are limited, the emission appears to be concentrated in regions near the top and bottom of the oval.

The pulsar location, determined by radio interferometric measurements made by Stappers, Gaensler, & Johnston (1999), is marked by a cross and lies near the bottom of the emission region. The dashed square indicates the region shown in SIS images (Figs. 1 [*bottom left*]–1 [*bottom right*]). The two ellipses represent the 95% and 99% positional error boxes of the γ-ray source 3EG J1048−5840 (Hartman et al. 1999; see below for additional discussion). Figure 1 (*top right*) displays the central region of the broadband (0.4–10 keV) image for the SIS, while Figures 1 (*bottom left*)

TABLE 1

ASTROMETRIC AND SPIN PARAMETERS FOR PSRs B1046−58 AND B1610−50

Parameter	PSR B1046−58	PSR B1610−50
Right ascension (J2000)[a]	10 48 12.6	16 14 11.6
Declination (J2000)[a]	−58 32 03.8	−50 48 01.9
Period, P (s)[b,c]	0.124	0.232
Period derivative, $\dot{P}$ (s s^{-1})[b]	95.9×10^{-15}	493×10^{-15}
Epoch of period (MJD)	49403.0	48658.0
Dispersion measure, DM (pc cm^{-3})[b]	129.09(1)	586(5)
Characteristic age, τ_c (kyr)	20.4	7.4
Spin-down luminosity, $\dot{E}$ (ergs s^{-1})	2.0×10^{36}	1.6×10^{36}
Distance, d (kpc)[d]	3.0	7.3
Column density, N_H (cm^{-2})[e]	$(0.40–1.4) \times 10^{22}$	$(1.8–2.2) \times 10^{22}$

[a] Radio positions, from Stappers et al. 1999, are uncertain by less than 0.″1. Units of right ascension are hours, minutes, and seconds, and units of declination are degrees, arcminutes, and arcseconds.

[b] Data obtained from the Taylor et al. 1995 pulsar catalog. This information is not used for the timing analysis of PSR B1046−58.

[c] Ephemeris for PSR B1046−58 was obtained from radio timing observations at the 64 m Parkes radio telescope in New South Wales, Australia.

[d] Derived from the Taylor & Cordes 1993 DM-distance model.

[e] Lower limits were derived from the Seward & Wang 1988 estimate of 10 neutral hydrogen atoms per free electron; upper limits were derived from Dickey & Lockman 1990.

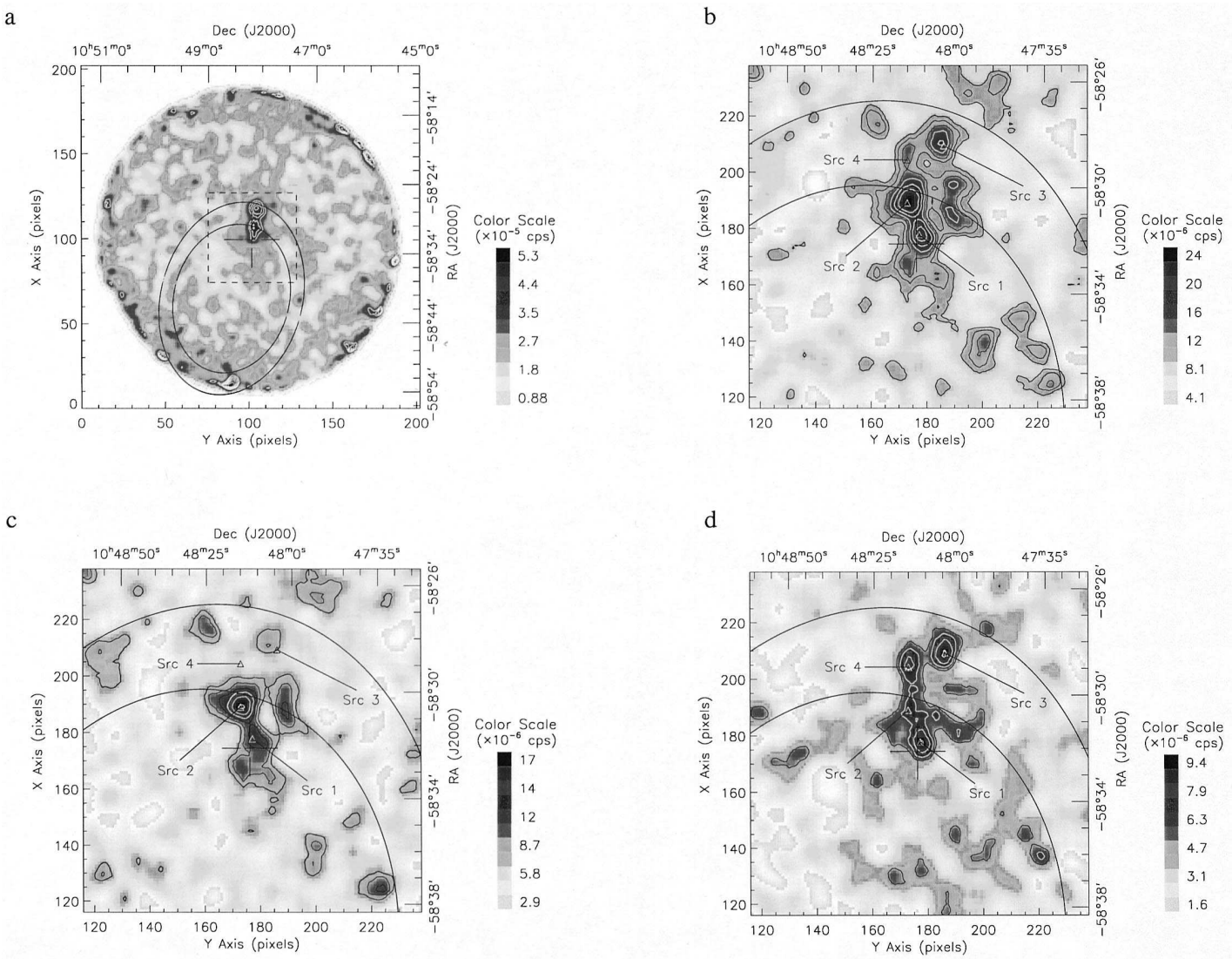

FIG. 1.—*ASCA* images of the PSR B1046−58 field: flat-fielded images of the region around the pulsar, whose location is marked by the cross. *Top left*: The broadband (0.8–12 keV) GIS image shows an oval-shaped region of X-ray emission with the pulsar located at its southern tip. The two ellipses represent the 95% and 99% error boxes for the γ-ray source 3EG J1048−5840. The dashed square delineates the SIS region displayed in the other three frames. *Top right*: The broadband (0.4–10 keV) SIS image clearly showing the three labeled sources embedded in a diffuse emission region. *Bottom left*: The soft-band SIS image (0.4–2 keV) revealing the soft, probably thermal nature of Src 2. Note that Srcs 1, 3, and 4 are very weak in this band. *Bottom right*: The hard-band (2–10 keV) SIS image showing the hard nature of Srcs 1, 3 and 4. We identify Src 1, offset 20″ from the radio position of PSR B1046−58 and the only source inside the 95% error circle of the pulsed γ-ray source 3EG J1048−5840, as the synchrotron nebula of PSR B1046−58. Contours approximately correspond to the 4 σ, 5 σ, 6 σ, 7 σ, 8 σ, and 9 σ levels. Count rates are in units of 10^{-5} counts s^{-1} $pixel^{-1}$ for the GIS and 10^{-6} counts s^{-1} $pixel^{-1}$ for the SIS.

and 1 (*bottom right*) show the soft-band (0.4–2 keV) and hard-band (2–10 keV) images for the same region. A cross marks the location of PSR B1046−58, and the arcs represent the errors ellipses for 3EG J1048−5840. Owing to its superior spatial performance, the SIS resolves the smooth emission seen by the GIS into four point sources (hereafter called Src 1, Src 2, Src 3, and Src 4) possibly situated in a region of faint diffuse emission.

The number of detected counts at the pulsar position is too small to fully resolve the familiar cross pattern of the X-ray telescope (XRT) PSF, as the morphology is dominated by Poisson fluctuations (see Hwang & Gotthelf 1997, § 2.2 for a discussion of the significance of peaks in similarly processed images). To estimate the significance of the detections, we ignore the complexities of the *ASCA* point-spread function and compare the number of photons collected from a small aperture centered on the source with that from a 12′–18′ diameter concentric annulus. The relatively small number of counts available in the source region makes the approximation reasonable. Unfortunately, the close proximity of the four sources complicates this analysis. An optimally sized[1] 4′ diameter aperture captures the majority of flux from the pulsar position as well as an undetermined amount of flux from neighboring sources, resulting in an overestimation of the pulsar's putative X-ray emission. Use of a smaller 2′ diameter aperture eliminates the contamination from the neighbors but neglects the flux in the broad wings ($\sim$3′) of the XRT PSF. Rather than artificially inflating the significance of a detection, we employ the 2′ diameter aperture with the understanding that our calculations

[1] Here, optimal refers to an aperture that maximizes the number of source counts captured within the extraction region, relative to the background contribution. See, e.g., Gotthelf & Kaspi (1998).

may underestimate the strength of a source. Using the formalism outlined by Gotthelf & Kaspi (1998), we estimate the detection significance (the signal-to-noise ratio, S/N) with an expression that accounts for both the source and background variance.

Table 2 presents relevant information for the four sources detected by both SIS detectors, including source positions, count rates, detection significance σ, and hardness ratio H, where $H \equiv$ counts (2–10 keV)/counts (0.4–2 keV). Src 1 is relatively hard ($H = 0.70 \pm 0.30$) and is strongly detected with a significance of 4.5 σ (44 background-subtracted counts). Src 2 is primarily soft ($H = 0.55 \pm 0.18$) and is strongly detected with a significance of 6.1 σ (69 background-subtracted counts). Src 3 is hard ($H = 1.55 \pm 0.82$) and has a significance of 3.9 σ (38 background-subtracted counts), while Src 4 is the hardest source ($H = 2.15 \pm 1.70$) and has a significance of 3.4 σ. In an attempt to reduce the influence of the diffuse emission and contamination from neighboring sources, centroid positions for Src 1, Src 3, and Src 4 were determined from analysis of the hard-band image in Figure 1 (*bottom right*), and the position for Src 2 was determined from the soft-band image in Figure 1 (*bottom left*). Combining the $\sim 15''$ centroid uncertainty for each source with the $\sim 20''$ revised pointing uncertainty (Gotthelf 1996)[2] for *ASCA* results in an overall source position uncertainty of order $\sim 25''$.

Src 1 lies 20″ from the radio position of the pulsar, within the positional errors. Assuming approximately four sources per square degree with comparable flux to Src 1 (Gendreau, Barcons, & Fabian 1998) and a SIS spatial resolution of 3′, we estimate the probability of a chance superposition of Src 1 with the pulsar's position to be of order 0.008. Src 2 lies 92″ away from the radio position, making it extremely unlikely that it is the X-ray counterpart of the pulsar.

Our images differ significantly from those produced by Kawai et al. (1998) from the same *ASCA* data. In particular, we do not find any evidence for a large ($\sim 10'$–$20'$) nebula around the pulsar. Our reanalysis of the GIS data and analysis of the SIS data provide support for emission from the pulsar (Src 1) that is unresolved by the *ASCA* PSF. Our disparate conclusions result primarily from the consideration of the SIS data with its superior spatial resolution, which shows that the oval-shaped region in the GIS image actually represents emission from the four sources resolved by the SIS. We have also employed different procedures in the GIS analysis. Specifically, we have used an exposure correction that removes the significant structure produced by the GIS support grid, and we have smoothed the data with a 3 × 3 boxcar function ($\sim 45''$ on a side) that approximates the core of the PSF.[3] When a much larger smoothing function is used, Poisson fluctuations, individual sources, and structure arising from the support grid (if not accounted for) can be blended into an apparent large, diffuse region of emission.

3.1.2. *ROSAT Data*

PSR B1046−58 was also observed on 1996 March 8 by the HRI (High Resolution Imager) on board *ROSAT* for 23 ks. Several point sources are clearly detected in the HRI FOV, but none is coincident with the position of the radio pulsar. The upper limit for a source at the radio position is less than 1×10^{-3} counts s^{-1}. This result is in disagreement with the detection of PSR B1046−58 with the HRI reported by Becker & Trümper (1997). A source is present, however, at $10^h48^m13^s.0$, $-58°30'44''$ (J2000), 80″ away from the pulsar's radio position. This *ROSAT* source is only 19″ away from SIS Src 2; given the apparently soft spectrum of Src 2 and the 25″ positional uncertainty of the *ASCA* sources, this suggests that they are the same source.

To try to identify this source (SIS Src 2), we searched several optical catalogs. The only coincident source, located $\sim 8''$ from the *ROSAT* position, was found in the Digital Sky Survey. Using the photometric calibration provided for the UK Schmidt Camera, we estimate a V magnitude of ~ 13.4. Positive identification of this optical source with the X-ray source detected by both *ROSAT* and *ASCA* requires spectroscopic data not presently available.

There are no other *ROSAT* sources spatially coincident with the remaining three SIS sources, which is not surprising given their harder spectra. Furthermore, no extended or diffuse emission is seen in the HRI data. This suggests that the faint diffuse emission seen in the SIS data may not be physically significant. One possible origin of this diffuse structure could be a blending of Poisson fluctuations with emission from the closely grouped point sources scattered by the broad PSF of the *ASCA* mirrors.

3.2. *Flux Estimation*

While the observations allow detection of the four sources, the low statistics prevent useful spectral analysis.

[2] http://legacy.gsfc.nasa.gov/docs/asca/coord/updatecoord.html.

[3] A similar procedure is also performed on the SIS data. The data is first rebinned ×4, then smoothed with a 5 × 5 boxcar function ($\sim 30''$ on a side).

TABLE 2

ASCA SIS Detection of PSR B1046−58 (0.4–10 keV band)

Source	Right Ascension (J2000)	Declination (J2000)	Count Rate ($\times 10^{-3}$ counts s^{-1})	Background Rate ($\times 10^{-3}$ counts s^{-1})	Hardness Ratio, H	Significance (σ)
Src 1.....	10 48 11.6	−58 31 46	3.99 ± 0.42	2.10 ± 0.04	0.70 ± 0.30	4.5
Src 2.....	10 48 5.1	−58 30 34	4.87 ± 0.43	2.18 ± 0.04	0.55 ± 0.18	6.1
Src 3.....	10 48 04.4	−58 28 26	3.62 ± 0.38	2.15 ± 0.05	1.48 ± 0.82	3.9
Src 4.....	10 48 15.1	−58 28 57	3.27 ± 0.38	2.21 ± 0.04	2.15 ± 1.70	3.4[a]

Notes.—The positions for Src 1, Src 3, and Src 4 were derived from the hard-band (2–10 keV) image; the position for Src 2 was derived from the soft-band (0.4–2 keV) image. Units of right ascension are hours, minutes, and seconds, and units of declination are degrees, arcminutes, and arcseconds. Total uncertainties in the source positions are $\sim 25''$. Count rate is the total source plus background count rate in an aperture centered on the source position. Background rate is the count rate in a 12′–18′ diameter annulus concentric with the source position, normalized to the source aperture. Refer to the text (§§ 3 and 4) for the definition of significance and further discussion on all the measured quantities. The hardness ratio H is defined as counts in the hard band (2–10 keV) divided by counts in the soft band (0.4–2 keV).

[a] This significance is for the 2–10 keV band. The broadband significance is 3.2 σ.

However, the hardness ratio H of the SIS sources and the lack of *ROSAT* counterparts for all but Src 2 give some information about the sources. Srcs 1, 3, and 4 must either be absorbed nonthermal sources or thermal sources with temperature of at least several keV. Src 2 appears to be either an intrinsically soft thermal source with temperature on order of 50 eV or a nonthermal source with a very steep power law that is undetectable above 2 keV in the SIS.

To extract a flux estimate for the X-ray counterpart of the pulsar, we assume a spectral shape and adjust the overall normalization to match the count rate[4] of Src 1. The canonical synchrotron nebula spectrum is characterized by a power law with photon index $\alpha = 2$, where $N(E) \propto E^{-\alpha}$ (see, e.g., Seward & Wang 1988; Becker & Trümper 1997). The neutral hydrogen column density $N_{\rm H}$ can be constrained by combining the Seward & Wang (1988) approximation of 10 neutral hydrogen atoms per free electron with the DM or by using the H I maps of Dickey & Lockman (1990). The former yields $N_{\rm H} = 4.0 \times 10^{21}$ cm^{-2}; the latter yields $N_{\rm H} < 1.4 \times 10^{22}$ cm^{-2}. We adopt a value between these two rough estimates of $N_{\rm H} = 5 \times 10^{21}$ cm^{-2}. After folding the spectral model through the instrument (SIS+XRT) response, we obtain an unabsorbed 2–10 keV flux of $(2.5 \pm 0.3) \times 10^{-13}$ ergs cm^{-2} s^{-1}. Folding these parameters through the *ROSAT* instrument response yields an expected HRI count rate of $(2.3 \pm 0.3) \times 10^{-3}$ counts s^{-1}, in rough agreement with the upper limit (1×10^{-3} counts s^{-1}) calculated above. The assumed spectral model and $N_{\rm H}$ also agree well with the observed hardness ratio.

3.3. *Timing*

We carried out a timing analysis for PSR B1046−58 using the combined data from the two GIS detectors. We selected events in the 2–10 keV band from a 4′ diameter aperture centered on Src 1, using data acquired at the high and medium data rates only. A total of 472 events, a large fraction ($\sim$60%) of which are due to the background, were folded using an ephemeris obtained from radio timing observations of PSR B1046−58 at the 64 m Parkes radio telescope in New South Wales, Australia. Table 1 contains the ephemeris. As the putative pulse shape is unknown, we employed the H-test (de Jager 1994) to search for pulsations. For a duty cycle $\delta = 0.5$, the 3 σ upper limit to the pulsed fraction is 0.31. For increasingly sharper pulse shapes of $\delta = 0.3$ and 0.1, the 3 σ upper limits are 0.22 and 0.12, respectively. The absence of pulsations from the GIS data is consistent with the work of Saito (1998).

4. PSR B1610−50

4.1. *Image Analysis*

Flat-fielded images were generated using the same prescription given in § 3.1. Figure 2 (*top left*) displays the resultant smoothed broadband (0.8–12 keV) image for the GIS. A cross marks the location of the pulsar determined from radio interferometric measurements (Stappers et al. 1999).[5] The dashed rectangle shows the SIS FOV. The black contours are an overlay of 843 MHz MOST observations of the supernova remnant Kes 32 (Whiteoak & Green 1996). The flux in the lower left-hand quadrant results from scattered emission from the X-ray–bright supernova remnant RCW 103, located 33′ from the GIS optical axis. The scattered intensity has the gradient and shape expected when the 12′ extent of the SNR is folded through the broad wings of the *ASCA* XRT (Gotthelf, Petre, & Hwang 1997). Examination of the soft-band (0.8–2 keV) and hard-band (2–12 keV) images in Figures 2 (*bottom left*) and 2 (*top right*) reveals that the contamination is largely confined to $E < 2$ keV, owing to the intrinsic spectral nature of RCW 103 and the decrease in the XRT scattering as a function of increasing energy. The SIS images have the same properties as the GIS images; for brevity, we only present the hard-band (2–10 keV) image in Figure 2 (*bottom right*).

We again ignore the complexities of the PSF and search for emission from the pulsar by comparing the number of photons collected from an (optimal) 4′ diameter aperture centered on the radio location and with those collected from a 6′–11′ diameter concentric annulus. By restricting our search to $E > 2$ keV, we greatly decrease the amount of scattered emission from RCW 103. Our choice of background annulus avoids emission from Kes 32 and roughly contains the same amount of scattered flux as the source aperture region, allowing a reliable significance calculation. No emission was detected by either the GIS or SIS, and the combined detection significance is below 2 σ.

As first noted by Kawai et al. (1998), the *ASCA* observation provides the first X-ray detection of the supernova remnant Kes 32. The low statistics prevent a detailed comparison of the X-ray emission with the elongated, shell-like radio morphology. To first order, the X-ray flux traces the radio intensity particularly along the western rim, as is evident in both the SIS and GIS images. The absence of X-ray emission from the direction of PSR B1610−50 contradicts a previous report of a large nebula powered by the pulsar (Kawai et al. 1998). Contamination from the scattered RCW 103 emission and effects of smoothing with a function larger than the size of the *ASCA* PSF (see the discussion in § 3.1.1) can account for the discrepancy.

Two additional sources are also present in the GIS data. At the top of the GIS FOV, the *Einstein* source 2E 1611.1−5018, a low-mass X-ray binary with J2000 coordinates $16^{\rm h}14^{\rm m}54^{\rm s}$, $-50°26'21''$, is clearly visible. This source is detected in both the hard and soft bands and was also detected by *ROSAT*. The second source, located south of the pulsar position and just outside the SIS FOV, is seen only above 2 keV. Data from both GIS detectors provide a 4.1 σ detection (47 background-subtracted counts). Its J2000 coordinates are $16^{\rm h}14^{\rm m}18^{\rm s}$, $-50°56'43''$, with a position uncertainty of $\sim$1′. The sourcelike enhancements along the southeastern edge of the GIS FOV result from scattered flux from RCW 103 and image processing artifacts.

4.2. *Flux Estimation*

The nondetection of PSR B1610−50 can be used to place an upper limit on the flux from the pulsar. Starting with the observed background rates[6] of 8.2×10^{-3} counts s^{-1}, we derive a 3 σ upper limit on the pulsar's count rate. We restrict our analysis to the GIS data, as these have a larger field of view for background estimation. We again use the canonical synchrotron nebula spectral model to estimate

[4] Here, the count rate is that determined in § 3.1, adjusted to account for the flux in the broad XRT wings that falls outside the extraction aperture.

[5] The interferometric pulsar position differs from the published catalog value by 57″ (Taylor et al. 1995, available at ftp://pulsar.princeton.edu/pub/catalog). No signal is present at either position.

[6] The background count rate is for an extraction region of radius 2′.

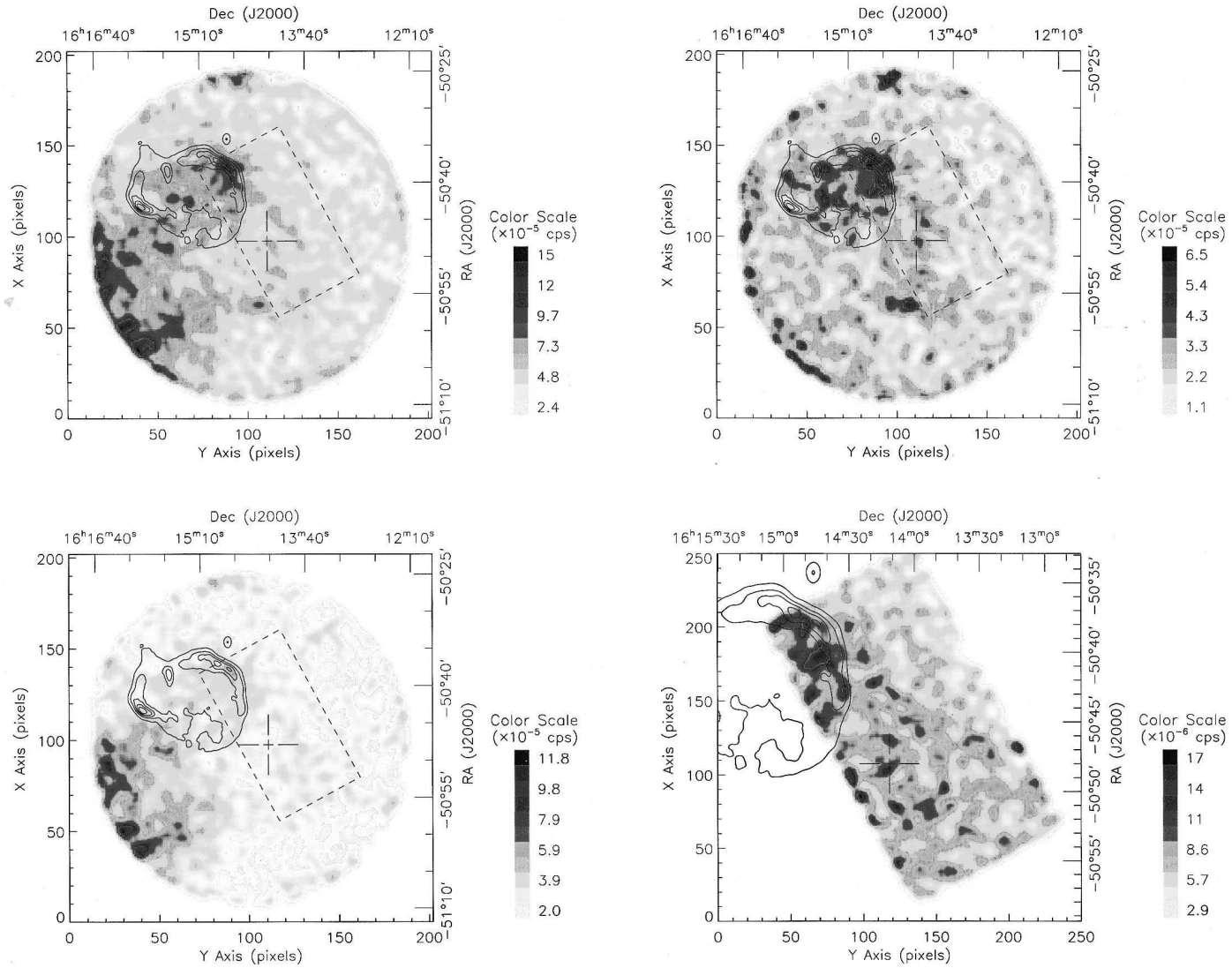

FIG. 2.—*ASCA* images of the PSR B1610−50 field: flat-fielded images of the region around the pulsar, whose location is marked by the cross. The dashed rectangle represents the SIS FOV, and the contours, corresponding to 0.04, 0.18, 0.31, 0.44, 0.57, and 0.70 Jy beam^{-1}, are from 843 MHz MOST observations of the supernova remnant Kes 32. *Top left*: The broadband (0.8–12 keV) GIS image of the PSR B1046−58 field. Scattered emission from the nearby supernova remnant RCW 103 is responsible for the large flux gradient that begins in the southeast FOV and extends to the edge of the SIS FOV. *Top right*: The hard-band (2–12 keV) GIS image shows enhanced emission that traces the radio emission from Kes 32. No significant flux is seen from the pulsar location. The previously known *Einstein* source 2E 1611.1−5018 is visible at the top of the FOV, while an unidentified source is located approximately due south of the pulsar position. *Bottom left*: The soft-band (0.8–2 keV) GIS image explicitly shows the extent of the scattered emission from RCW 103. Note the distinct *lack* of emission from Kes 32. *Bottom right*: The hard-band (2–10 keV) SIS image similarly shows the correspondence between the radio contours and X-ray emission and no emission from PSR B1610−50. Count rates are in units of 10^{-5} counts s^{-1} pixel^{-1} for the GIS and 10^{-6} counts^{-1} s^{-1} pixel^{-1} for the SIS.

the flux and constrain the column density following the approach taken in § 3.2. We adopt a value of $N_{\rm H} = 2 \times 10^{22}$ cm^{-2}, consistent with the Seward & Wang estimate and the Dickey & Lockman upper limit. After folding the spectrum through the appropriate instrument response (GIS+XRT), we calculate a 3 σ upper limit to the unabsorbed 2–10 keV flux of 1.5×10^{-13} ergs cm^{-2} s^{-1}.

5. DISCUSSION

The importance of the detection of weak emission from PSR B1046−58 and the nondetection of PSR B1610−50 is most readily understandable in the context of the growing body of work on the X-ray properties of young ($\tau_c = P/2\dot{P} < 10^5$ yr) rotation-powered neutron stars. More than 20 of these objects have been detected, with three distinct physical processes responsible for the observed X-ray flux.

Thermal emission can result either from the initial cooling of a young neutron star (e.g., Ögelman 1995 and references therein) or from polar-cap reheating in older pulsars (e.g., Becker & Trümper 1993). If the heated cap sweeps across our line of sight, this emission may also be pulsed, as in the case of the Vela pulsar, which has an 11% pulsed fraction in the 0.1–2.4 keV band (Ögelman, Finley, & Zimmermann 1993), or PSR B1055−52, which has a similar pulsed fraction that varies with energy in the 0.1–10 keV band (Ögelman & Finley 1993; Greiveldinger et al. 1996). The blackbody emission is independent of the spin-down luminosity $\dot{E}$.

Nonthermal magnetospheric emission, produced either in the polar cap or outer gap regions, is responsible for the classic "pulsar phenomenon," characterized by sharp pulsations of high pulsed fraction. The most famous example is

the Crab pulsar, whose pulsed X-ray spectrum is characterized by a power law with photon index 2 (Toor & Seward 1974). The energy for pulsed magnetospheric emission originates from the spin-down and is seen from pulsars having high $\dot{E}$ at the extremes of the age distribution, from young ($\tau_c < 10^4$ yr) pulsars such as the Crab, PSR B1509−58, and the two LMC pulsars PSR B0540−69 and PSR J0537−6910, to old ($\tau_c > 10^7$ yr) millisecond pulsars such as PSR J0437−4715 and PSR B1821−24 (Seward & Harnden 1982; Seward, Harnden, & Helfand 1984a; Marshall et al. 1998; Becker & Trümper 1993; Saito et al. 1997).

The pulsar can have an associated synchrotron nebula, the observable evidence for the channeling of the vast store of rotational kinetic energy into a wind of relativistic particles. Such nebulae arise when the pulsar wind is confined and is subsequently shocked by the surrounding ISM, e.g., the nebulae produced by the Crab and Vela pulsars and PSR B1509−58 (Brinkmann, Aschenbach, & Langmeier 1985 and references therein; Harnden et al. 1985; Ögelman & Zimmermann 1989; Seward et al. 1984b, Brazier & Becker 1997 and references therein).

5.1. *PSR B1046−58*

For an age of 20 kyr, cooling models (see, e.g., Ögelman 1995) predict thermal emission from PSR B1046−58 to have an effective surface temperature of at most $kT \approx 120$ eV and a maximum bolometric luminosity of 2.3×10^{33} ergs s^{-1}. Assuming a 10 km neutron star radius, a 3 kpc distance, and $N_{\rm H} \approx 5 \times 10^{21}$ cm^{-2}, the *ASCA* count rates should be no higher than 8×10^{-3} counts s^{-1} (SIS) and 2×10^{-3} counts s^{-1} (GIS). While these rates are comparable to the observed rates from the pulsar direction (refer to Table 2), the predicted count rate should fall to undetectable levels above 1.5 keV, in contradiction with the observations. Thus, cooling thermal emission cannot produce the observed flux from PSR B1046−58.

The apparently hard spectrum of the radiation suggests a nonthermal origin, either from the magnetosphere or from a synchrotron nebula. Magnetospheric emission is strongly pulsed, and given the upper limits on pulsations from the GIS data, it is extremely unlikely that magnetospheric emission contributes any significant fraction of the flux. Deeper observations could reveal pulsations arising from either the magnetosphere or the modulation of thermal, surface emission.

The most probable source of emission is synchrotron radiation powered by a relativistic pulsar wind. The most famous pulsar wind nebula surrounds the Crab pulsar (Rees & Gunn 1974; Kennel & Coroniti 1984; Emmering & Chevalier 1987; Gallant & Arons 1994). In pulsar wind nebulae, the wind of relativistic electrons and positrons (and possibly heavy ions; Hoshino et al. 1992) are confined, accelerated at the reverse shock, and radiate synchrotron emission. Using the flux range calculated in § 3.2 the 2–10 keV luminosity is $L_{\rm X} = (2.7 \pm 0.3) \times 10^{32} d_{3.0}^2$ ergs s^{-1}, where $d_{3.0}$ is the distance in units of 3.0 kpc. The conversion efficiency ϵ of the spin-down luminosity $\dot{E}$ into *ASCA*-band emission is $\epsilon = (1.3 \pm 0.1) \times 10^{-4}$.

The $\sim 3'$ broad wings of the *ASCA* PSF severely limit detailed morphological studies of the synchrotron nebula. As the emission appears consistent with a point source, we can place a conservative $3'$ diameter upper limit on its angular extent. The limited spectral resolution also prevents us from considering whether the faint extended emission surrounding the four SIS sources could be the supernova remnant associated with PSR B1046−58, a reasonable speculation given the pulsar's apparent youth. Ultimately, the nature of the extended emission and its possible relation to PSR B1046−58 will be resolved only through observations with sufficiently high spatial and spectral resolution that would, for example, allow the detection of emission line features commonly found in other young supernova remnants.

5.2. *3EG J1048−5840*

On a list ranked by $\dot{E}/d^2$, a parameter that has proved to be an excellent indicator of γ-ray detectability, PSR B1046−58 is the ninth, with six of the eight sources higher being γ-ray pulsars. PSR B1046−58 thus represents an excellent candidate for observable high-energy γ-ray emission. Indeed, in a companion paper, Kaspi et al. (2000) suggest an association between PSR B1046−58 and the unidentified high-energy γ-ray source 3EG J1048−5840 based on the detection of significant pulsations from the γ-ray source at the radio pulsar period.

Identifying X-ray counterparts to unidentified EGRET sources is a useful way of significantly reducing the uncertainty in the position of the γ-ray source, on the assumption that the source spectrum extends into the X-ray band, true for both blazars and pulsars (e.g., Kubo et al. 1998; Becker & Trümper 1997). In Figure 1 (*top left*), we show the 95% and 99% confidence spatial contours of 3EG J1048−5840 overlaid on the broadband GIS image (Hartman et al. 1999). Fortunately, the archival *ASCA* observation covers the entire γ-ray error box. The four detected *ASCA* sources discussed above (§ 3.1) are the only significant X-ray sources in the field; one or more of them is therefore probably the source of the γ-ray emission.

The *ASCA* source nearest (within the 95% contour) the best-fit 3EG J1048−5840 position is Src 1, which we have identified with PSR B1046−58. It therefore represents the most likely counterpart to 3EG J1048−5840, and supports the evidence presented by Kaspi et al. (2000). Src 2, within the 95% region, was shown (§ 3.2) to have a soft spectrum, hence is unlikely to be the γ-ray source counterpart. The unidentified hard-spectrum Src 3 lies well outside the 95% contour but just within the 99% contour, so we cannot formally preclude its being the counterpart. However, were it the counterpart, it would most likely have to be a *second* young, energetic pulsar in the field, as it has no obvious radio counterpart, and hence cannot be a blazar, since all known γ-ray–emitting blazars are bright radio sources (Mattox et al. 1997).

5.3. *PSR B1610−50*

The nondetection of PSR B1610−50 obviously prevents a study of the emission characteristics of the pulsar. However, derived upper limits are important for studying and understanding the X-ray properties of young rotation-powered pulsars as a population, particularly given this pulsar's place in age-space between the youngest Crab-like pulsars and the older Vela-like pulsars.

At an age $\tau = 7.4$ kyr, the Ögelman (1995) cooling model predicts thermal emission from the surface of the neutron star with a characteristic temperature $kT \approx 130$ eV. With the large column density toward the pulsar and its distance, though, the absorbed flux in the 2–10 keV band would be $F_{\rm X} = 2.1 \times 10^{-17}$ ergs s^{-1} cm^{-2}, orders of magnitude

below the *ASCA* detectability threshold. Pulsed magnetospheric emission is also expected to be present, given that pulsars with similar $\dot{E}$ exhibit pulsed nonthermal emission. However, as the total flux in the pulsed radiation is usually less than that from a synchrotron nebula, we used only the nonthermal X-ray emission expected from the nebula in our calculation of an upper flux limit in § 3.3. For a flux limit $F_X < 1.5 \times 10^{-13}$ ergs s^{-1} cm^{-2} and a distance of 7.3 kpc, the 2–10 keV luminosity is $L_X < 9.6 \times 10^{32} d_{7.3}^2$ ergs s^{-1}. The conversion efficiency ϵ of the spin-down luminosity $\dot{E}$ into *ASCA*-band emission is $\epsilon < 6.1 \times 10^{-4}$.

If we assume that PSR B1610−50 has an X-ray–emitting synchrotron nebula, it is likely to be confined by ram pressure, as there is no evidence from X-ray or radio observations of a confining shell (i.e., SNR) around the pulsar (Green 1998).[7] Relying on the work of Arons & Tavani (1993) and others, Gotthelf & Kaspi (1998 and references therein) show that the cooling efficiency for relativistic pairs of positrons and electrons is

$$\epsilon \equiv \frac{t_f}{t_s} = 3.6 \times 10^{-4} \left(\frac{\sigma}{0.005}\right) \left(\frac{\rho}{1 \text{ H atom}}\right)^{1/2} \times \left(\frac{v}{100 \text{ km s}^{-1}}\right) \left(\frac{\gamma}{10^8}\right), \quad (1)$$

where t_f and t_s are the timescales for the pulsar wind flow and synchrotron cooling, σ is the ratio of magnetic energy flux to the kinetic energy flux of the wind ($\sigma \approx 0.005$ for the Crab pulsar; Kennel & Coroniti 1984), ρ is the ambient density, v is the pulsar's velocity, and γ is the postshock pair Lorentz factor (Thompson et al. 1995). The bolometric luminosity in synchrotron emission for the highest energy pairs is $L_s \approx \epsilon \dot{E}$. If PSR B1610−50 has wind properties similar to those of the Crab pulsar, the velocity must be $\lesssim 170$ km s^{-1} given the absence of X-ray emission. This velocity is inconsistent with an association between the pulsar and Kes 32. Unless the pulsar resides in an extremely underdense region, i.e., $\rho \lesssim 5.4 \times 10^{-3}$ cm^{-3}, or has very different wind properties compared to the Crab pulsar, PSR B1610−50 does not have the transverse velocity suggested by Caraveo (1993).

5.4. L_X-$\dot{E}$ Relationships

The luminosity measured for PSR B1046−58 and the upper limit derived for PSR B1610−50 can be considered within the context of two previously determined empirical correlations between spin-down luminosity $\dot{E}$ and X-ray luminosity L_X: the Seward & Wang (1988, hereafter SW88) relationship derived from *Einstein* data (0.2–4.0 keV band), $\log L_X = 1.39 \log \dot{E} - 16.6$, and the Becker & Trümper (1997, hereafter BT97) relationship derived from *ROSAT* data (0.1–2.4 keV band), $L_X = 10^{-3} \dot{E}$. To estimate the scatter associated with these models, we have computed the rms, defined here to be the square root of the variance, using the data presented by the authors in their papers. For the *Einstein* model, the rms scatter is a factor of ~ 7, while for the *ROSAT* model, the rms scatter is a factor of ~ 4. For PSR B1046−58, SW88 predicts $7.2^{51}_{1.0} \times 10^{33}$ ergs s^{-1}, compared to the observed $(5.0 \pm 0.5) \times 10^{32}$ ergs s^{-1}, while BT97 predicts $2.0^{8.0}_{0.5} \times 10^{33}$, compared to the observed $(5.3 \pm 0.5) \times 10^{32}$ ergs s^{-1}. In both cases, the relationships overestimate L_X by factors of at least several. For PSR B1610−50, SW88 predicts $5.3^{37}_{0.8} \times 10^{33}$ ergs s^{-1}, compared with the derived upper limit 1.3×10^{33} ergs s^{-1}, while BT97 predicts $1.6^{6.4}_{0.4} \times 10^{33}$, compared with the derived upper limit 1.4×10^{33} ergs s^{-1}. For this pulsar, the derived upper limits lie within the range of predicted values.

One possible source of error is the distance derived from the Taylor & Cordes (1993) DM-d model. Distances are uncertain to $\sim$25%–50%, translating to a potential error as a large as a factor of ~ 3 when converting flux to luminosity. Increasing the distance by $\sim$25%–50% leads to a corresponding increase in L_X and helps improve the agreement between model and observation. The discrepancies between model and observation also suggests that the current L_X-$\dot{E}$ relationships, while certainly illustrating a correlation between spin-down and X-ray luminosity, may overlook important factors such as the pulsar's velocity or the ISM conditions in its vicinity.

6. CONCLUSIONS

We have analyzed archival *ASCA* X-ray data for pulsars PSR B1046−58 and PSR B1610−50. We have detected emission from PSR B1046−58 with a 4.5 σ significance, the emission most likely arising from a synchrotron nebula. We estimate the 2–10 keV unabsorbed flux to be $F_X = (2.5 \pm 0.3) \times 10^{-13}$ ergs cm^{-2} s^{-1}, assuming a distance $d = 3.0$ kpc. The data show no evidence for pulsation, with pulsed fraction less than 31% at the 90% confidence limit for a duty cycle of 50%. The synchrotron nebula is the only hard source within the 95% error ellipse of the previously unidentified γ-ray source 3EG J1048−5840 and one of only two hard sources within the 99% error ellipse. The X-ray data, coupled with γ-ray pulsations discovered by Kaspi et al. (2000), strengthen the case for identifying PSR B1046−58 as one of the few radio pulsars known to emit pulsed γ-rays. We detect no emission from PSR B1610−50 and place an upper limit on the 2–10 keV unabsorbed flux $F_X < 1.5 \times 10^{-13}$ ergs cm^{-2} s^{-1}. This flux limit argues that the pulsar's velocity $v \lesssim 170$ km s^{-1}, providing evidence against the association between by PSR B1610−50 and Kes 32 claimed by Caraveo (1993).

The flux-derived luminosities for both pulsars are below those predicted by the Seward & Wang (1988) and Becker & Trümper (1997) L_X-$\dot{E}$ relationship, particularly for PSR B1046−58. The differences may represent the intrinsic limitations of the current empirically derived L_X-$\dot{E}$ relationships, which do not consider parameters such as ambient density and pulsar velocity.

The unresolved nebula powered by PSR B1046−58 and the nondetection from PSR B1610−50 contradict previous reports by Kawai et al. (1998) of large ($\sim 10'$–$20'$) nebulae associated with these pulsars. These observations also demonstrate the difficulties associated with analyzing and interpreting current hard X-ray ($E > 2$ keV) imaging data. The upcoming launch of the *Chandra X-Ray Observatory*, with its unparalleled resolution ($\sim 0''.5$) and hard-band sensitivity, and *XMM*, with its good spatial resolution ($\sim 8''$) and large collecting area, should improve this situation considerably.

We thank B. Gaensler for providing the radio images of the PSR B1046−58 and PSR B1610−50-Kes 32 fields and for useful discussion. We thank M. Bailes, R. Manchester, and R. Pace for acquiring radio timing data for PSR

[7] http://mrao.cam.ac.uk/surveys/snrs.

B1046−58 at the 64 m Parkes radio telescope in New South Wales, Australia. We thank R. Hartman for providing information on 3EG J1048−5840 prior to publication. We thank W. Becker for discussion on the analysis of the *ROSAT* observations of PSR B1046−58. Finally, we thank the anonymous referee for useful comments and suggestions that improved this paper. We have used the NASA maintained HEASARC web site extensively for archival data retrieval and subsequent analysis. M. Pivovaroff is supported in part by NASA under contract NASA-37716.

REFERENCES

Arons, J., & Tavani, M. 1993, ApJ, 403, 249
Becker, W., & Trümper, J. 1993, Nature, 365, 528
———. 1997, A&A, 326, 682
Brazier, K. T. S., & Becker, W. 1997, MNRAS, 284, 335
Brinkmann, W., Aschenbach, B., & Langmeier, A. 1985, Nature, 313, 662
Caraveo, P. A. 1993, ApJ, 415, L111
Cheng, A. F. 1983, ApJ, 275, 790
de Jager, O. C. 1994, ApJ, 436, 239
Dickey, J. M., & Lockman, F. J. 1990, ARA&A, 28, 215
Emmering, R. T., & Chevalier, R. A. 1987, ApJ, 321, 334
Finley, J. P., Srinivasan, R., & Park, S. 1996, ApJ, 466, 938
Gallant, Y. A., & Arons, J. 1994, ApJ, 435, 230
Gendreau, K. C., Barcons, X., & Fabian, A. C. 1998, MNRAS, 297, 41
Gotthelf, E. V. 1996, Improved *ASCA* Sky Coordinates (Greenbelt: NASA Goddard Space Flight Center)
Gotthelf, E. V., & Kaspi, V. M. 1998, ApJ, 497, L29
Gotthelf, E. V., Petre, R., & Hwang, U. 1997, ApJ, 487, L175
Green, D. A. 1998, A Catalogue of Galactic Supernova Remnants (1998 September version) (Cambridge: Mullard Radio Astronomy Observatory)
Greiveldinger, C., et al. 1996, ApJ, 465, L35
Harnden, F. R., Grant, P. D., Seward, F. D., & Kahn, S. M. 1985, ApJ, 299, 828
Hartmann, R. C., et al. 1999, ApJS, 123, 79
Hoshino, M., Arons, J., Gallant, Y. A., & Langdon, A. B. 1992, ApJ, 390, 454
Hwang, U., & Gotthelf, E. V. 1997, ApJ, 475, 665
Johnston, S., Lyne, A. G., Manchester, R. N., Kniffen, D. A., D'Amico, N., Lim, J., & Ashworth, M. 1992, MNRAS, 255, 401
Kaspi, V. M., Lackey, J., Mattox, J., Manchester, R. N., & Bailes, M. 2000, ApJ, 528, 445
Kawai, N., Tamura, K., & Saito, Y. 1998, Adv. Space Res., 21, 213
Kennel, C. F., & Coroniti, F. V. 1984, ApJ, 283, 710
Kubo, H., Takahashi, T., Madejski, G., Tashiro, M., Makino, F., Inoue, S., & Takahara, F. 1998, ApJ, 504, 693
Lyne, A. G., & Lorimer, D. R. 1994, Nature, 369, 127
Marshall, F. E., Gotthelf, E. V., Zhang, W., Middleditch, J., & Wang, Q. D. 1998, ApJ, 499, L179
Mattox, J. R., Schachter, J., Molnar, L., Hartman, R. C., & Patnaik, A. R. 1997, ApJ, 481, 95
Ögelman, H. 1995, in The Lives of the Neutron Stars, ed. A. Alpar, Ü Kiziloğlu, & J. van Paradijs (NATO ASI Series; Dordrecht: Kluwer), 101
Ögelman, H., & Finley, J. P. 1993, ApJ, 413, L31
Ögelman, H., Finley, J. P., & Zimmermann, H. U. 1993, Nature, 361, 136
Ögelman, H., & Zimmermann, H.-U. 1989, A&A, 214, 179
Rees, M. J., & Gunn, J. E. 1974, MNRAS, 167, 1
Romani, R. W., Cordes, J. M., & Yadigaroglu, I.-A. 1997, ApJ, 484, L137
Saito, Y. 1998, Ph.D. thesis, Univ. of Tokyo
Saito, Y., Kawai, N., Kamae, T., Shibata, S., & Dotani, T. 1997, ApJ, 477, 37
Seward, F. D., & Harnden, F. R. 1982, ApJ, 256, L45
Seward, F. D., Harnden, F. R., & Helfand, D. J. 1984a, ApJ, 287, L19
Seward, F. D., Harnden, F. R., Szymkowiak, A., & Swank, J. 1984b, ApJ, 281, 650
Seward, F. D., & Wang, Z.-U. 1988, ApJ, 332, 199
Stappers, B. W., Gaensler, B. M., & Johnston, S. 1999, MNRAS, 308, 609
Tanaka, Y., Inoue, H., & Holt, S. S. 1994, PASJ, 46, L37
Taylor, J. H., & Cordes, J. M. 1993, ApJ, 411, 674
Taylor, J. H., Manchester, R. N., Lyne, A. G., & Camilo, F. 1995, unpublished
Thompson, D. J., et al. 1995, ApJS, 101, 259
Toor, A., & Seward, F. D. 1974, AJ, 79, 995
Wang, Q. D., & Gotthelf, E. V. 1998, ApJ, 494, 623
Wang, Q. D., Li, Z.-Y., & Begelman, M. C. 1993, Nature, 364, 127
Whiteoak, J. B. Z., & Green, A. J. 1996, A&AS, 118, 329